ARBITRARY LAGRANGIAN-EULERIAN (ALE)-BASED FINITE ELEMENT METHODS FOR RIGID SOLIDS IMMERSED IN FLUIDS

Stevens Paz, Fabricio S. Sousa and Gustavo C. Buscaglia

Departamento de Matemática Aplicada e Estatística, Instituto de Ciências Matemáticas e de Computação (ICMC), Universidade de São Paulo, Campus de São Carlos, Caixa Postal 668, 13560-970 São Carlos, São Paulo, Brazil, espeisan@usp.br, http://icmc.usp.br

Keywords: Arbitrary Lagrangian-Eulerian schemes, fluid-solid interaction, finite element method.

Abstract. Arbitrary Lagrangian-Eulerian approaches are widely used in CFD, especially in multi-physics problems. They involve two tasks, namely the computation of the physical variables (velocity, stress, force, torque, etc.) and the determination of a suitable mesh deformation. We consider here a decoupled treatment of these two tasks, with high-order temporal schemes obtained by extrapolation, as discussed in F. Montefuscolo et.al. (*J Comp Phys*, 278:133-147, 2014) for capillary problems. Extensions of these schemes to fluid/rigid-body interaction are presented, adopting a variational formulation made popular by R. Glowinski et.al. in their work on Fictitious Domain Methods (*J Comp Phys*, 169:363-426, 2001). The Arbitrary Lagrangian-Eulerian discretization turns the variational fluid-solid problem into a Differential-Algebraic Equation system for which several schemes, with different orders of accuracy, are implemented and evaluated. Special attention is dedicated to issues of stability, which is a fundamental obstacle towards the effective simulation of microfluidic fluid-solid interaction problems.

1 INTRODUCTION

Fluid-solid interaction phenomena has been of great interest to engineers and applied mathematicians' research since it appears in several industrial applications, like sedimentation processes and agglomeration of particles. The coupling between the continuous phase (fluid) dynamics and the rigid body motion has been examined by Glowinski et al. (2001) supposing a solid filled with fluid and enforcing the rigidity through Lagrange multipliers over a fixed domain. Parallel, Hu et al. (2001) showed that decoupling the fluid from the solid motion at each time step could be unstable, and propose an explicit-implicit method in which the mesh is updated explicitly and the coupled fluid and solid velocities are calculated implicitly. This fluid-solid coupling is obtained by virtue of surface forces that appear naturally over the weak formulation of the problem.

The mentioned fluid-solid system requires to select conditions over the fluid-solid (also for fluid-fluid) interfaces, in particular Stokes no-slip condition has been widely used (Day, 1990). However, slip velocities could be generated by concentration gradients or catalyzed chemical reactions throughout interfaces resulting in (diffusio-) phoretic swimming, even without net body forces acting on the solid (Ruckenstein and Dunn, 1977; Golestanian et al., 2005; Jülicher and Prost, 2009; Popescu et al., 2010). Now, in the presence of electric fields or temperature gradients, particles immersed in fluids can respond due to electrophoretic (Saintillan, 2008; Khair and Squires, 2009) or thermophoretic phenomena (Yang et al., 2014), respectively. In this work, a preset slip velocity is impose over the solids interface, which allows us to recover no-slip conditions by vanishing this velocity.

High-order Arbitrary Lagrangian-Eulerian (ALE) schemes for capillary flows proposed by Montefuscolo et al. (2014) are used here for solving the fluid-solid interaction problem with slip velocity. Initially, the spatial variables are discretized by finite elements, transforming the continuous problem into a Differential-Algebraic Equation (DAE) system depending on the nodal coefficients of fluid velocity, fluid pressure, mesh velocity and mesh position. Then, the temporal discretization step is accomplished in such a way that mesh variables could be solved aside from the fluid ones, this by means of mesh extrapolations techniques, and finite differences of several orders.

2 THE FLUID-SOLID INTERACTION EQUATIONS

A domain $\Omega \subset \mathbb{R}^d$, $d = 2$ or 3, is filled with a viscous incompressible fluid of density ρ_f, viscosity μ, velocity $\mathbf{u}$ and pressure p, surrounding N rigid bodies denoted by $B^K(t) \subset \Omega$, $t \in [0, T)$, of mass M_K, $1 \le K \le N$, respectively (Figure 1). The fluid velocity field $\mathbf{u}$ and pressure p satisfy the Navier-Stokes equations in ALE formulation,

$$\begin{cases} \rho_f \left(\partial_t^* \mathbf{u} + (\mathbf{u} - \mathbf{v}) \cdot \nabla \mathbf{u} \right) = \nabla \cdot \boldsymbol{\sigma} + \mathbf{F} \\ \nabla \cdot \mathbf{u} = 0 \end{cases} \quad \text{in } \Omega_f(t), \ t \in (0, T), \tag{1}$$

where $\Omega_f(t) := \Omega \setminus \bigcup\limits_{K=1}^{N} \overline{B^K(t)}$, with suitable boundary and initial conditions,

$$\begin{aligned} \mathbf{u}(\mathbf{x}, t) &= \mathbf{u}_D(\mathbf{x}, t) && \text{on } \partial\Omega \times (0, T), \\ \mathbf{u}(\mathbf{x}, 0) &= \mathbf{u}_0(\mathbf{x}) && \text{in } \Omega. \end{aligned} \tag{2}$$

Here, $\mathbf{F}$ is a body force per unit volume, the Cauchy stress tensor is defined by $\boldsymbol{\sigma} = -p\mathbf{I} + 2\mu D\mathbf{u}$ with $D\mathbf{u} := \frac{1}{2} \left[\nabla \mathbf{u} + (\nabla \mathbf{u})^T \right]$, $\mathbf{I}$ is the identity tensor, and $\mathbf{u}_D$, $\mathbf{u}_0$ are given functions, usually
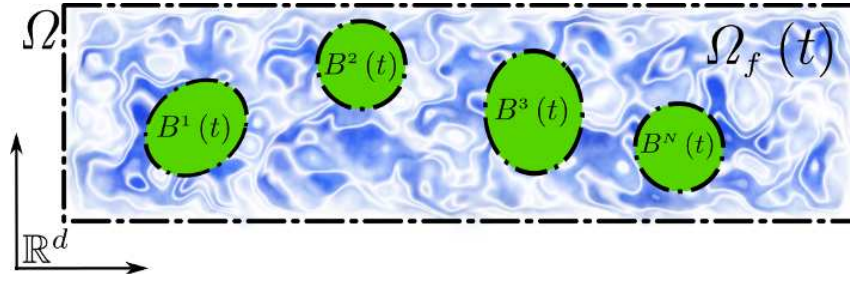
Figure 1: Schematic of N solids immersed in a fluid

set as zero (no-slip conditions and zero initial velocities). The ALE derivative, $\partial_t^* := \partial_t + \mathbf{v} \cdot \nabla$, results from introducing an arbitrary referential, used to describe the mesh movement with the arbitrary mesh velocity $\mathbf{v}$, defined as

$$\frac{d\mathbf{x}}{dt} = \mathbf{v}, \tag{3}$$

taking $\mathbf{x}(\cdot, t)$ as a mapping from the arbitrary referential domain to the spatial domain.

The evolution of the K-th rigid body, with center of mass $\mathbf{x}_g^K$, is modeled by the Newton-Euler equations

$$\begin{cases} M_K \dfrac{d\mathbf{V}^K}{dt} = M_K \mathbf{g} - \displaystyle\int_{\partial B^K} \boldsymbol{\sigma}\mathbf{n} \, dS \\[3mm] \mathbb{I}^K \dfrac{d\boldsymbol{\omega}^K}{dt} + \boldsymbol{\omega}^K \times \mathbb{I}^K \boldsymbol{\omega}^K = -\displaystyle\int_{\partial B^K} \left(\mathbf{x} - \mathbf{x}_g^K\right) \times \boldsymbol{\sigma}\mathbf{n} \, dS \end{cases} \quad \text{on } (0, T), \tag{4}$$

completed by the initial positions and velocities of the solids,

$$B^K(0) = B_0^K, \quad \mathbf{x}_g^K(0) = \mathbf{x}_{g0}^K, \quad \mathbf{V}^K(0) = \mathbf{V}_0^K, \quad \boldsymbol{\omega}^K(0) = \boldsymbol{\omega}_0^K, \quad \forall K = 1, \ldots, N. \tag{5}$$

The translational velocity $\mathbf{V}^K = \sum_{i=1}^d V_i^K \mathbf{e}_i$ is defined as

$$\frac{d\mathbf{x}_g^K}{dt} = \mathbf{V}^K, \tag{6}$$

this is, the velocity of the center of mass, and the pseudovector $\boldsymbol{\omega}^K = \sum_{i=1}^3 \omega_i^K \mathbf{e}_i$ corresponds to the angular velocity of the K-th solid, being $\{\mathbf{e}_i\}_{i=1}^d$ the canonical basis of $\mathbb{R}^d$. Also, the unitary normal vector $\mathbf{n}$, at ∂B^K, points into B^K, and the inertia tensor $\mathbb{I}^K = \left(I_{ij}^K\right)_{1 \le i,j \le 3}$ of the K-th body, with respect to its center of mass, is given by

$$I_{ij}^K = \int_{B^K} \rho_K \left(\mathbf{r}^K \cdot \mathbf{r}^K - \delta_{ij} r_i^K r_j^K\right) \, d\mathbf{x}$$

where $\mathbf{r}^K = \sum_{i=1}^d r_i^K \mathbf{e}_i := \mathbf{x} - \mathbf{x}_g^K$ and δ_{ij} being a Kronecker delta.

In the two-dimensional case (and for spheres solid shapes) the term $\boldsymbol{\omega}^K \times \mathbb{I}^K \boldsymbol{\omega}^K$ vanishes in (4), so we rewrite this system as

$$\mathbb{M}^K \frac{d\mathbf{Z}^K}{dt} = \mathbf{F}^K, \tag{7}$$

where $\mathbb{M}^K := \operatorname{diag}(M_K, M_K, I_{33,K})$ is a mass matrix, $\mathbf{Z}^K := \left(V_1^K, V_2^K, \omega_3^K\right)^T$ is vector of velocities, and $\mathbf{F}^K$ a vector of forces.

3 GLOBAL VARIATIONAL FORMULATION AND ALE DISCRETIZATION

The rigid solid dynamics results from restricting the movement degrees of freedom to the *infinitesimal generator functions* given by translations and rotations. This is translated into the velocity expression

$$\mathbf{u}^K(\mathbf{x}, t) = \mathbf{V}^K(t) + \boldsymbol{\omega}^K(t) \times (\mathbf{x} - \mathbf{x}_g^K(t)), \quad \forall \mathbf{x} \in \overline{B^K(t)}, \tag{8}$$

for each K-th solid at time $t \in [0, T]$. These movements can be enriched allowing other degrees of freedom coming from new generators like deformations of the solid through vibration modes. However, for the particular case of interaction between fluids and rigid solids, we focus in the formula (8) that can be rewritten as

$$\mathbf{u}^K(\mathbf{x}, t) = \mathbb{H}^K(\mathbf{x}, t) \mathbf{Z}^K(t), \quad \forall \mathbf{x} \in \overline{B^K(t)},$$

being $\mathbf{Z}^K \in \mathbb{R}^{\frac{d(d+1)}{2}}$ the vector formed by translational and angular velocities, and the operator $\mathbb{H}^K(\cdot, t)$ acting over $\mathbf{Z}^K(t)$ in such a way that the expression (8) is accomplished for all $t \in [0, T]$. Regarding consistency of notation in two-dimensional cases, as was mentioned for (7), the vector $\mathbf{Z}^K \in \mathbb{R}^3$ is made of the two translational velocity components and the third component of the angular velocity pseudovector.

A tangent velocity field $\mathbf{u}_s^K$, named slip velocity, defined over fluid-solid interfaces may appear as a response of solids to catalyzed chemical reactions sources, or concentration gradients, acting on the solid's surfaces. The contribution of this phenomena, known as diffusiophoretic, and others like thermophoretic and electrophoretic, is introduced to the fluid-solid system as the condition

$$\mathbf{u}(\mathbf{x}, t) = \mathbf{u}^K(\mathbf{x}, t) + \mathbf{u}_s^K(\mathbf{x}, t), \quad \forall \mathbf{x} \in \partial B^K(t),$$

that couples the systems (1) and (4).

Based on the global variational formulation presented by Glowinski et al. (2001), we introduce the function spaces

$$\begin{aligned}
W_{\mathbf{u}_s}(t) = \Big\{ (\mathbf{w}, \mathbf{W}) : &\mathbf{w} \in \left(H^1(\Omega_f(t))\right)^d, \, \mathbf{w} = \mathbf{0} \text{ on } \partial\Omega, \, \mathbf{W} = \left(\mathbf{W}^K\right)_{K=1}^N, \\
&\mathbf{W}^K = \left(\mathbf{Y}^K, \boldsymbol{\theta}^K\right), \, \mathbf{Y}^K \in \mathbb{R}^d, \, \boldsymbol{\theta}^K \in \mathbb{R}^3, \\
&\mathbf{w}(\mathbf{x}, t) = \mathbf{Y}^K(t) + \boldsymbol{\theta}^K(t) \times \left(\mathbf{x} - \mathbf{G}^K(t)\right) + \mathbf{u}_s^K(\mathbf{x}, t) \text{ on } \partial B^K(t), \\
&1 \leq K \leq N \Big\},
\end{aligned}$$

and $Q(t) = L^2(\Omega(t))/\mathbb{R}$, in particular, W_0, which results taking $\mathbf{u}_s \equiv 0$, is formed by the functions satisfying that the fluid velocity is equal to the solid velocity at the interfaces, this is, a no-slip condition. Besides, the Newton-Euler equations (4) for the rigid bodies are transformed into natural conditions through the surface forces, these ones acting over fluid-solid interfaces and placing its contributions into the weak formulation coming from the momentum equations. Then, applying the virtual power principle to the fluid-solid system, it yields the problem:

Find $\left(\mathbf{u}\left(\cdot,t\right),\mathbf{Z}\left(t\right)\right)\in W_{\mathbf{u}_s}\left(t\right),\mathbf{Z}^K=\left(\mathbf{V}^K,\boldsymbol{\omega}^K\right),p\left(t\right)\in Q\left(t\right)$, for almost all $t\in[0,T)$, such that,

$$\rho_f\int_{\Omega_f(t)}\left[\partial_t^*\mathbf{u}+\left(\left(\mathbf{u}-\mathbf{v}\right)\cdot\nabla\right)\mathbf{u}\right]\cdot\mathbf{w}+2\mu\int_{\Omega_f(t)}D\left(\mathbf{u}\right):D\left(\mathbf{w}\right)$$

$$-\int_{\Omega_f(t)}p\nabla\cdot\mathbf{w}+\sum_{K=1}^N M_K\frac{d\mathbf{V}^K}{dt}\cdot\mathbf{Y}^K+\sum_{K=1}^N\left(\mathbb{I}^K\frac{d\boldsymbol{\omega}^K}{dt}+\boldsymbol{\omega}^K\times\mathbb{I}^K\boldsymbol{\omega}^K\right)\cdot\boldsymbol{\theta}^K$$

$$=\int_{\Omega_f(t)}\mathbf{F}\cdot\mathbf{w}+\sum_{K=1}^N M_K\mathbf{g}\cdot\mathbf{Y}^K,$$

for all $\left(\mathbf{w}\left(\cdot,t\right),\mathbf{W}\left(t\right)\right)\in W_0\left(t\right),\mathbf{W}^K=\left(\mathbf{Y}^K,\boldsymbol{\theta}^K\right)$, and

$$-\int_\Omega q\nabla\cdot\mathbf{u}=0,$$

for all $q\left(t\right)\in Q\left(t\right)$, with conditions (2), (5), (8) and the evolution of center of mass (6).

A complete discretization for the previous variational formulation is obtained by initially using the finite element method (FEM) to spatial variables, which generates a DAE system, and then several schemes of different orders are used for discretization in time. For the following equations we will take $\mathbf{F}=\rho_f\mathbf{g}$, this is, the gravitational force.

Given a triangulation $\mathcal{T}_h\left(t\right)$ of Ω, being h the characteristic mesh length, which defines a discrete domain $\Omega_h\left(t\right)$, the functions $\mathbf{u}$ and p are approximated by

$$\mathbf{u}_h\left(\mathbf{x},t\right)=\sum_{j\in\eta_U}\mathcal{N}^j\left(\mathbf{x},t\right)\mathbf{u}^j\left(t\right)+\sum_{K=1}^N\sum_{J\in\eta_K}\mathcal{N}^J\left(\mathbf{x},t\right)\left[\mathbb{H}^K\left(\mathbf{x}^J,t\right)\mathbf{Z}^K\left(t\right)+\mathbf{u}_s^K\left(\mathbf{x}^J,t\right)\right],$$

$$p_h\left(\mathbf{x},t\right)=\sum_{k\in\eta_P}\mathcal{M}^k\left(\mathbf{x},t\right)p^k\left(t\right),$$

(9)

in finite dimensional subspaces $W_{\mathbf{u}_s,h}\subset W_{\mathbf{u}_s}$ e $Q_h\subset Q$, with polynomial basis on each $K\in\mathcal{T}_h$, via the shape functions $\mathcal{N}^j$, $j\in\eta$, $\mathcal{M}^k$, $k\in\eta_P$, and the variable coefficients $\mathbf{u}^j,\mathbf{Z}^J,p^k$ satisfying the nodal value property, noticing that the operator $\mathbb{H}^K$ is evaluated at the mesh node $\mathbf{x}^J$, $J\in\eta_K$. Here, the set of global velocity nodes indexes $\eta=\cup_{K=1}^N\eta_K\cup\eta_U$ is splitted into the index set η_K of solid velocity nodes at the K-th solid interface, and the remaining fluid velocity nodes indexes η_U. The set of pressure nodes indexes is denoted by η_P. The function $\mathbf{u}_h$ is completely determine by the coefficients $\mathbf{u}^j$ and $\mathbf{Z}^K$, therefore the fluid velocity at any mesh point $\mathbf{x}_J\in\overline{B^K}$ can be recovered by applying the operator $\mathbb{H}^K\left(\mathbf{x}_J,\cdot\right)$ to $\mathbf{Z}^K$ plus the slip velocity at that point.

Taking the test functions $\left(\mathbf{w}_h,\mathbf{W},q_h\right)\in W_{0h}\times Q_h$, with $W_{0h}\subset W_0$, we obtain the set of equations

$$\rho_f\int_{\Omega_f(t)}\left[\partial_t^*\mathbf{u}_h+\left(\left(\mathbf{u}_h-\mathbf{v}_h\right)\cdot\nabla\right)\mathbf{u}_h\right]\cdot\left(\mathcal{N}^i\mathbf{e}_c\right)+2\mu\int_{\Omega_f(t)}D\left(\mathbf{u}_h\right):D\left(\mathcal{N}^i\mathbf{e}_c\right)$$

$$-\int_{\Omega_f(t)}p_h\nabla\cdot\left(\mathcal{N}^i\mathbf{e}_c\right)=\rho_f\int_{\Omega_f(t)}\mathbf{g}\cdot\left(\mathcal{N}^i\mathbf{e}_c\right)$$

(10)

for each $i \in \eta_U$, $1 \leq c \leq d$, being $\{\mathbf{e}_c\}_{c=1}^d$ the canonical basis of $\mathbb{R}^d$,

$$
\sum_{I \in \eta_K} \left(\rho_f \int_{\Omega_f(t)} [\partial_t^* \mathbf{u}_h + ((\mathbf{u}_h - \mathbf{v}_h) \cdot \nabla) \, \mathbf{u}_h] \cdot \left(\mathcal{N}^I \mathbb{H}^{K,I} \tilde{\mathbf{e}}_C \right) \right.
$$
$$
\left. + 2\mu \int_{\Omega_f(t)} D \left(\mathbf{u}_h \right) : D \left(\mathcal{N}^I \mathbb{H}^{K,I} \tilde{\mathbf{e}}_C \right) - \int_{\Omega_f(t)} p_h \nabla \cdot \left(\mathcal{N}^I \mathbb{H}^{K,I} \tilde{\mathbf{e}}_C \right) \right) \quad (11)
$$
$$
+ \left(\mathbb{M}^K \frac{d\mathbf{Z}^K}{dt} + \tilde{\mathbf{i}}^K \right) \cdot \tilde{\mathbf{e}}_C = \rho_f \int_{\Omega_f(t)} \mathbf{g} \cdot \left(\mathcal{N}^I \mathbb{H}^{K,I} \tilde{\mathbf{e}}_C \right) + M_K \tilde{\mathbf{g}} \cdot \tilde{\mathbf{e}}_C
$$

for each $1 \leq K \leq N$, $1 \leq C \leq \frac{d(d+1)}{2}$, being $\{\tilde{\mathbf{e}}_C\}_{C=1}^{\frac{d(d+1)}{2}}$ the canonical basis of $\mathbb{R}^{\frac{d(d+1)}{2}}$, and

$$
- \int_{\Omega(t)} \mathcal{M}^k \nabla \cdot \mathbf{u}_h = 0, \quad (12)
$$

for each $k \in \eta_P$, where

$$
\mathbb{M}^K := \begin{pmatrix} M_K \mathbf{I} & \\ & \mathbb{I}^K \end{pmatrix}, \quad \tilde{\mathbf{i}}^K := \begin{pmatrix} \mathbf{0} \\ \boldsymbol{\omega}^K \times \mathbb{I}^K \boldsymbol{\omega}^K \end{pmatrix}, \quad \tilde{\mathbf{g}} := \begin{pmatrix} \mathbf{g} \\ \mathbf{0} \end{pmatrix}, \quad \mathbf{0} \in \mathbb{R}^{\frac{d(d+1)}{2}},
$$

and $\mathbb{H}^{K,I} := \mathbb{H}^K \left(\mathbf{x}^I, \cdot \right)$. As already mentioned, when $d = 2$, the vector $\tilde{\mathbf{i}}^K$ vanishes and the matrix $\mathbb{M}^K$ takes the same form used in (7). The ALE derivative, as showed by Montefuscolo et al. (2014), can be calculated through the expression

$$
\partial_t^* \mathbf{u}_h = \sum_{j \in \eta_U} \mathcal{N}^j \frac{d\mathbf{u}^j}{dt} + \sum_{K=1}^N \sum_{J \in \eta_K} \mathcal{N}^J \frac{d}{dt} \left[\mathbb{H}^{K,J} \mathbf{Z}^K + \mathbf{u}_s^{K,J} \right], \quad (13)
$$

where $\mathbf{u}_s^{K,J} := \mathbf{u}_s^K \left(\mathbf{x}^J, t \right)$, and remembering that the triangulation moves with time (3), then the nodal velocities defined as

$$
\mathbf{v}^j := \frac{d\mathbf{x}^j}{dt}, \quad (14)
$$

induces the velocity field $\mathbf{v}_h \left(\mathbf{x}, t \right) = \sum_{j \in \eta} \mathcal{N}^j \left(\mathbf{x}, t \right) \mathbf{v}^j \left(t \right)$, corresponding to an approximation of the mesh velocity $\mathbf{v}$ in the space W_{0h}. This arbitrary mesh velocity comes from solving a linear elasticity problem (Montefuscolo et al., 2014), namely

$$
\nabla \cdot \left(\lambda_e \left(\nabla \cdot \mathbf{v}_h \right) \mathbf{I} + 2\mu_e D\mathbf{v}_h \right) = \mathbf{0} \quad \text{in } \Omega_h, \quad (15)
$$

subject to

$$
\left(\mathbf{v}_h \left(\mathbf{x}^j, t \right) - \mathbf{u}_h \left(\mathbf{x}^j, t \right) \right) \cdot \mathbf{n}_h \left(\mathbf{x}^j, t \right) = 0, \quad \mathbf{x}^j \in \partial \Omega_{hf} \left(t \right),
$$

for some discrete normal $\mathbf{n}_h$, with Lamé parameters λ_e, μ_e chosen as $\lambda_e = -\mu_e = E$, where E is element-wise constant and equal to the inverse of the element volume.

The new set of algebraic equations, resulting from a discrete variational formulation applied to (15), is given by

$$
\int_{\Omega(t)} \left[\lambda_e \left(\nabla \cdot \mathbf{v}_h \right) \mathbf{I} + 2\mu_e D\mathbf{v}_h \right] : D \left(\mathcal{N}^i \mathbf{e}_c \right) = 0, \quad (16)
$$

for each $i \in \eta$, $1 \leq c \leq d$ which, together with the set of equations (10), (11), (12) and (14), complete a DAE system in the unknowns $\boldsymbol{U} \left(t \right) = \{\mathbf{u}^j \left(t \right)\}$, $\boldsymbol{Z} \left(t \right) = \left\{ \mathbf{Z}^J \left(t \right) \right\}$, $\boldsymbol{P} \left(t \right) = \left\{ p^k \left(t \right) \right\}$, $\boldsymbol{X} \left(t \right) = \{\mathbf{x}^j \left(t \right)\}$ and $\boldsymbol{V} \left(t \right) = \{\mathbf{v}^j \left(t \right)\}$.

2171

4   TIME DISCRETIZATION

Given a function f, we denote its θ-interpolation at $n + \theta$ as $f^{n+\theta} \coloneqq \theta f^n + (1 - \theta) f^{n+\theta}$, where f^n is the approximation of f at time level $t^n = n\Delta t$ with time step $\Delta t = t^{n+1} - t^n$ and $\theta \in [0, 1]$. Also, we use the backward difference operators defined by Montefuscolo et al. (2014), namely

$$
\begin{aligned}
\delta_1 f^{n+1} &= f^{n+1} - f^n, \\
\delta_2 f^{n+1} &= \frac{3}{2} f^{n+1} - 2f^n + \frac{1}{2} f^{n-1}, \\
\delta_3 f^{n+1} &= \frac{11}{6} f^{n+1} - 3f^n + \frac{3}{2} f^{n-1} - \frac{1}{3} f^{n-2}.
\end{aligned}
\tag{17}
$$

Then, after applying a temporal discrete operator (17) to the equations (10), (11), (12), (14) and (16), we can define the respective residuals

$$
\begin{aligned}
\mathcal{F}u_c^i\big(\boldsymbol{U}^{n+\theta}, \boldsymbol{Z}^{n+\theta}, \boldsymbol{P}^{n+\theta}, \boldsymbol{X}^{n+\theta}, \boldsymbol{V}^{n+\theta}\big) \coloneqq{}& \rho_f \int_{\Omega_f^{n+\theta}} \left[\frac{1}{\Delta t} \delta_l^* \mathbf{u}_h^{n+\theta} \right] \cdot \big(\mathcal{N}^{i,n+\theta} \mathbf{e}_c\big) \\
&+ \rho_f \int_{\Omega_f^{n+\theta}} \big[\big((\mathbf{u}_h^{n+\theta} - \mathbf{v}_h^{n+\theta}) \cdot \nabla \big) \mathbf{u}_h^{n+\theta} \big] \cdot \big(\mathcal{N}^{i,n+\theta} \mathbf{e}_c\big) \\
&+ 2\mu \int_{\Omega_f^{n+\theta}} D\big(\mathbf{u}_h^{n+\theta}\big) : D\big(\mathcal{N}^{i,n+\theta} \mathbf{e}_c\big) \\
&- \int_{\Omega_f^{n+\theta}} p_h^{n+\theta} \nabla \cdot \big(\mathcal{N}^{i,n+\theta} \mathbf{e}_c\big) - \rho_f \int_{\Omega_f^{n+\theta}} \mathbf{g}^{n+\theta} \cdot \big(\mathcal{N}^{i,n+\theta} \mathbf{e}_c\big),
\end{aligned}
$$

for each $i \in \eta_U$ and $1 \le c \le d$,

$$
\begin{aligned}
\mathcal{F}z_C^K\big(\boldsymbol{U}^{n+\theta}, \boldsymbol{Z}^{n+\theta}, \boldsymbol{P}^{n+\theta}, \boldsymbol{X}^{n+\theta}, \boldsymbol{V}^{n+\theta}\big) \coloneqq{}& \sum_{I \in \eta_K} \rho_f \int_{\Omega_f^{n+\theta}} \left[\frac{1}{\Delta t} \delta_l^* \mathbf{u}_h^{n+\theta} \right] \cdot \big(\mathcal{N}^{K,n+\theta} \mathbb{H}^{K,I,n+\theta} \tilde{\mathbf{e}}_C\big) \\
&+ \sum_{I \in \eta_K} \rho_f \int_{\Omega_f^{n+\theta}} \big[\big((\mathbf{u}_h^{n+\theta} - \mathbf{v}_h^{n+\theta}) \cdot \nabla \big) \mathbf{u}_h^{n+\theta} \big] \cdot \big(\mathcal{N}^{K,n+\theta} \mathbb{H}^{K,I,n+\theta} \tilde{\mathbf{e}}_C\big) \\
&+ \sum_{I \in \eta_K} 2\mu \int_{\Omega_f^{n+\theta}} D\big(\mathbf{u}_h^{n+\theta}\big) : D\big(\mathcal{N}^{K,n+\theta} \mathbb{H}^{K,I,n+\theta} \tilde{\mathbf{e}}_C\big) \\
&- \sum_{I \in \eta_K} \int_{\Omega_f^{n+\theta}} p_h^{n+\theta} \nabla \cdot \big(\mathcal{N}^{K,n+\theta} \mathbb{H}^{K,I,n+\theta} \tilde{\mathbf{e}}_C\big) \\
&- \sum_{I \in \eta_K} \rho_f \int_{\Omega_f^{n+\theta}} \mathbf{g}^{n+\theta} \cdot \big(\mathcal{N}^{K,n+\theta} \mathbb{H}^{K,I,n+\theta} \tilde{\mathbf{e}}_C\big) \\
&+ \left(\mathbb{M}^K \frac{1}{\Delta t} \delta_l \mathbf{Z}^{K,n+1} + \tilde{\mathbf{i}}^{K,n+\theta} - M_K \tilde{\mathbf{g}}^{n+\theta} \right) \cdot \tilde{\mathbf{e}}_C,
\end{aligned}
$$

for each $1 \le K \le N$ and $1 \le C \le \frac{d(d+1)}{2}$,

$$
\mathcal{F}P^k\big(\boldsymbol{U}^{n+\theta}, \boldsymbol{Z}^{n+\theta}, \boldsymbol{P}^{n+\theta}, \boldsymbol{X}^{n+\theta}, \boldsymbol{V}^{n+\theta}\big) \coloneqq -\int_{\Omega^{n+\theta}} \mathcal{M}^{k,n+\theta} \nabla \cdot \mathbf{u}_h^{n+\theta},
$$

for each $k \in \eta_P$, and

$$\mathcal{F}v_c^i\big(\boldsymbol{U}^{n+\theta}, \boldsymbol{X}^{n+\theta}, \boldsymbol{V}^{n+\theta}\big) := \int_{\Omega^{n+\theta}} \left[\lambda_e \left(\nabla \cdot \mathbf{v}_h^{n+\theta}\right) \mathbf{I} + 2\mu_e D\mathbf{v}_h^{n+\theta}\right] : D\left(\mathcal{N}^i \mathbf{e}_c\right) - \mathcal{B}_c^i\big(\boldsymbol{U}^{n+\theta}\big)$$

for each $i \in \eta$ and $1 \le c \le d$. In these definitions the operator δ_l^* acts as a backward difference for the ALE derivative (13) over the nodal coefficients $\mathbf{u}^j$ and $\mathbb{H}^{K,J}\mathbf{Z}^K + \mathbf{u}_s^{K,J}$, for $l = 1, 2, 3$. Also, the operator $\mathcal{B}_c^i$ is construct in such a way that the mesh velocity coincides with the solid velocity at interfacial nodes. So, we obtain the non-linear system of equations

$$\frac{1}{\Delta t}\delta_l \boldsymbol{X}^{n+1} - \boldsymbol{V}^{n+\theta} = 0, \tag{18a}$$

$$\mathcal{F}v_c^i\big(\boldsymbol{U}^{n+\theta}, \boldsymbol{X}^{n+\theta}, \boldsymbol{V}^{n+\theta}\big) = 0, \quad i \in \eta, 1 \le c \le d, \tag{18b}$$

$$\mathcal{F}u_c^i\big(\boldsymbol{U}^{n+\theta}, \boldsymbol{Z}^{n+\theta}, \boldsymbol{P}^{n+\theta}, \boldsymbol{X}^{n+\theta}, \boldsymbol{V}^{n+\theta}\big) = 0, \quad i \in \eta_U, 1 \le c \le d, \tag{18c}$$

$$\mathcal{F}z_C^K\big(\boldsymbol{U}^{n+\theta}, \boldsymbol{Z}^{n+\theta}, \boldsymbol{P}^{n+\theta}, \boldsymbol{X}^{n+\theta}, \boldsymbol{V}^{n+\theta}\big) = 0, \quad 1 \le K \le N, 1 \le C \le \tfrac{d(d+1)}{2}, \tag{18d}$$

$$\mathcal{F}P^k\big(\boldsymbol{U}^{n+\theta}, \boldsymbol{Z}^{n+\theta}, \boldsymbol{P}^{n+\theta}, \boldsymbol{X}^{n+\theta}, \boldsymbol{V}^{n+\theta}\big) = 0, \quad k \in \eta_P, \tag{18e}$$

for the unknowns $\boldsymbol{U}^{n+1}$, $\boldsymbol{Z}^{n+1}$, $\boldsymbol{P}^{n+\theta}$, $\boldsymbol{X}^{n+1}$ and $\boldsymbol{V}^{n+1}$ (the vector $\boldsymbol{P}^{n+\theta}$ is taken as an unknown itself), noticing that the vectorial equation (18a) is the discretization of (14) for all nodal positions.

We will present, coming up next, some numerical methods based on those proposed by Montefuscolo et al. (2014), in which, extrapolation techniques are explored in order to decouple the geometry and mesh velocity calculations made in (18a) and (18b), from the fluid-solid interaction equations given by (18c), (18d) and (18e).

4.1 Midpoint rule/Adams-Bashforth method (MR/AB)

This method results from taking $\theta = \frac{1}{2}$ and $l = 1$, then

$$\frac{1}{\Delta t}\delta_1 \boldsymbol{X}^{n+1} - \boldsymbol{V}^{n+\frac{1}{2}} = 0, \tag{19a}$$

$$\mathcal{F}v_c^i\big(\hat{\boldsymbol{U}}^{n+\frac{1}{2}}, \hat{\boldsymbol{X}}^{n+\frac{1}{2}}, \boldsymbol{V}^{n+\frac{1}{2}}\big) = 0, \quad i \in \eta, 1 \le c \le d, \tag{19b}$$

$$\mathcal{F}u_c^i\big(\boldsymbol{U}^{n+\frac{1}{2}}, \boldsymbol{Z}^{n+\frac{1}{2}}, \boldsymbol{P}^{n+\frac{1}{2}}, \boldsymbol{X}^{n+\frac{1}{2}}, \boldsymbol{V}^{n+\frac{1}{2}}\big) = 0, \quad i \in \eta_U, 1 \le c \le d, \tag{19c}$$

$$\mathcal{F}z_C^K\big(\boldsymbol{U}^{n+\frac{1}{2}}, \boldsymbol{Z}^{n+\frac{1}{2}}, \boldsymbol{P}^{n+\frac{1}{2}}, \boldsymbol{X}^{n+\frac{1}{2}}, \boldsymbol{V}^{n+\frac{1}{2}}\big) = 0, \quad 1 \le K \le N, 1 \le C \le \tfrac{d(d+1)}{2}, \tag{19d}$$

$$\mathcal{F}P^k\big(\boldsymbol{U}^{n+\frac{1}{2}}, \boldsymbol{Z}^{n+\frac{1}{2}}, \boldsymbol{P}^{n+\frac{1}{2}}, \boldsymbol{X}^{n+\frac{1}{2}}, \boldsymbol{V}^{n+\frac{1}{2}}\big) = 0, \quad k \in \eta_P. \tag{19e}$$

Here, the extrapolated geometry and velocity are calculated with the Adams-Bashforth-like formulae

$$\hat{\boldsymbol{X}}^{n+\frac{1}{2}} = \frac{3}{2}\boldsymbol{X}^n - \frac{1}{2}\boldsymbol{X}^{n-1}, \quad \hat{\boldsymbol{U}}^{n+\frac{1}{2}} = \frac{3}{2}\boldsymbol{U}^n - \frac{1}{2}\boldsymbol{U}^{n-1},$$

allowing us to obtain the unknown mesh velocity $\boldsymbol{V}^{n+\frac{1}{2}}$ from (19b), which can be placing into (19a) to calculate the mesh position $\boldsymbol{X}^{n+1}$. Finally, with this information plugged into the non-linear system of equations (19c), (19d) and (19e) it is possible to find $\boldsymbol{U}^{n+1}$, $\boldsymbol{Z}^{n+1}$ and $\boldsymbol{P}^{n+\frac{1}{2}}$ and proceed to the next time step.

4.2 BDF2/extrapolated BDF2 method (BDF2/BDF2E)

In this case we set $\theta = 1$ and $l = 2$, then

$$\frac{1}{\Delta t}\delta_2 \boldsymbol{X}^{n+1} - \boldsymbol{V}^{n+1} = 0, \tag{20a}$$

$$\mathcal{F}v_c^i\big(\hat{\boldsymbol{U}}^{n+1}, \hat{\boldsymbol{X}}^{n+1}, \boldsymbol{V}^{n+1}\big) = 0, \quad i \in \eta, 1 \le c \le d, \tag{20b}$$

$$\mathcal{F}u_c^i\big(\boldsymbol{U}^{n+1}, \boldsymbol{Z}^{n+1}, \boldsymbol{P}^{n+1}, \boldsymbol{X}^{n+1}, \boldsymbol{V}^{n+1}\big) = 0, \quad i \in \eta_U, 1 \le c \le d, \tag{20c}$$

$$\mathcal{F}z_C^K\big(\boldsymbol{U}^{n+1}, \boldsymbol{Z}^{n+1}, \boldsymbol{P}^{n+1}, \boldsymbol{X}^{n+1}, \boldsymbol{V}^{n+1}\big) = 0, \quad 1 \le K \le N, 1 \le C \le \frac{d(d+1)}{2}, \tag{20d}$$

$$\mathcal{F}P^k\big(\boldsymbol{U}^{n+1}, \boldsymbol{Z}^{n+1}, \boldsymbol{P}^{n+1}, \boldsymbol{X}^{n+1}, \boldsymbol{V}^{n+1}\big) = 0, \quad k \in \eta_P, \tag{20e}$$

with the extrapolations

$$\hat{\boldsymbol{X}}^{n+1} = 2\boldsymbol{X}^n - \boldsymbol{X}^{n-1}, \quad \hat{\boldsymbol{U}}^{n+1} = 2\boldsymbol{U}^n - \boldsymbol{U}^{n-1},$$

to calculate the mesh velocity $\boldsymbol{V}^{n+1}$ which is in the time step $n+1$ different from the previous method.

4.3 BDF2/Adams-Bashforth method (BDF2/AB)

Now we put $\theta = \frac{1}{2}$ and $l = 1$ for the geometry and mesh velocity set of equations, and $\theta = 1$ and $l = 2$ for the Navier-Stokes part, this is,

$$\frac{1}{\Delta t}\delta_1 \boldsymbol{X}^{n+1} - \boldsymbol{V}^{n+\frac{1}{2}} = 0, \tag{21a}$$

$$\mathcal{F}v_c^i\big(\hat{\boldsymbol{U}}^{n+\frac{1}{2}}, \hat{\boldsymbol{X}}^{n+\frac{1}{2}}, \boldsymbol{V}^{n+\frac{1}{2}}\big) = 0, \quad i \in \eta, 1 \le c \le d, \tag{21b}$$

$$\mathcal{F}u_c^i\big(\boldsymbol{U}^{n+1}, \boldsymbol{Z}^{n+1}, \boldsymbol{P}^{n+1}, \boldsymbol{X}^{n+1}, \boldsymbol{V}^{n+1}\big) = 0, \quad i \in \eta_U, 1 \le c \le d, \tag{21c}$$

$$\mathcal{F}z_C^K\big(\boldsymbol{U}^{n+1}, \boldsymbol{Z}^{n+1}, \boldsymbol{P}^{n+1}, \boldsymbol{X}^{n+1}, \boldsymbol{V}^{n+1}\big) = 0, \quad 1 \le K \le N, 1 \le C \le \frac{d(d+1)}{2}, \tag{21d}$$

$$\mathcal{F}P^k\big(\boldsymbol{U}^{n+1}, \boldsymbol{Z}^{n+1}, \boldsymbol{P}^{n+\frac{1}{2}}, \boldsymbol{X}^{n+1}, \boldsymbol{V}^{n+1}\big) = 0, \quad k \in \eta_P, \tag{21e}$$

with the extrapolations

$$\hat{\boldsymbol{X}}^{n+\frac{1}{2}} = \frac{3}{2}\boldsymbol{X}^n - \frac{1}{2}\boldsymbol{X}^{n-1}, \quad \hat{\boldsymbol{U}}^{n+\frac{1}{2}} = \frac{3}{2}\boldsymbol{U}^n - \frac{1}{2}\boldsymbol{U}^{n-1}.$$

To calculate the mesh velocity $\boldsymbol{V}^{n+1}$ from the just found intermediate velocity $\boldsymbol{V}^{n+\frac{1}{2}}$, we use

$$\boldsymbol{V}^{n+1} = 2\boldsymbol{V}^{n+\frac{1}{2}} - \boldsymbol{V}^n.$$

4.4 BDF3/extrapolated BDF3 method (BDF3/BDF3E)

For this method we choose $\theta = 1$ and $l = 3$, then

$$\frac{1}{\Delta t}\delta_3 \boldsymbol{X}^{n+1} - \boldsymbol{V}^{n+1} = 0, \tag{22a}$$

$$\mathcal{F}v_c^i\big(\hat{\boldsymbol{U}}^{n+1}, \hat{\boldsymbol{X}}^{n+1}, \boldsymbol{V}^{n+1}\big) = 0, \quad i \in \eta, 1 \le c \le d, \tag{22b}$$

$$\mathcal{F}u_c^i\big(\boldsymbol{U}^{n+1}, \boldsymbol{Z}^{n+1}, \boldsymbol{P}^{n+1}, \boldsymbol{X}^{n+1}, \boldsymbol{V}^{n+1}\big) = 0, \quad i \in \eta_U, 1 \le c \le d, \tag{22c}$$

$$\mathcal{F}z_C^K\big(\boldsymbol{U}^{n+1}, \boldsymbol{Z}^{n+1}, \boldsymbol{P}^{n+1}, \boldsymbol{X}^{n+1}, \boldsymbol{V}^{n+1}\big) = 0, \quad 1 \le K \le N, 1 \le C \le \frac{d(d+1)}{2}, \tag{22d}$$

$$\mathcal{F}P^k\big(\boldsymbol{U}^{n+1}, \boldsymbol{Z}^{n+1}, \boldsymbol{P}^{n+1}, \boldsymbol{X}^{n+1}, \boldsymbol{V}^{n+1}\big) = 0, \quad k \in \eta_P, \tag{22e}$$

with the extrapolations

$$\hat{\boldsymbol{X}}^{n+1} = 3\boldsymbol{X}^n - 3\boldsymbol{X}^{n-1} + \boldsymbol{X}^{n-2}, \quad \hat{\boldsymbol{U}}^{n+1} = 3\boldsymbol{U}^n - 3\boldsymbol{U}^{n-1} + \boldsymbol{U}^{n-2}.$$

4.5   Basic staggered scheme (BSS)

For this method we choose $\theta = 1$ and $l = 1$, then

$$\frac{1}{\Delta t}\delta_1 \boldsymbol{X}^{n+1} - \boldsymbol{V}^n = 0, \tag{23a}$$

$$\mathcal{F}\boldsymbol{v}_c^i\big(\boldsymbol{U}^n, \boldsymbol{X}^n, \boldsymbol{V}^n\big) = 0, \quad i \in \eta, 1 \le c \le d, \tag{23b}$$

$$\mathcal{F}\boldsymbol{u}_c^i\big(\boldsymbol{U}^{n+1}, \boldsymbol{Z}^{n+1}, \boldsymbol{P}^{n+1}, \boldsymbol{X}^{n+1}, \boldsymbol{V}^n\big) = 0, \quad i \in \eta_U, 1 \le c \le d, \tag{23c}$$

$$\mathcal{F}\boldsymbol{z}_C^K\big(\boldsymbol{U}^{n+1}, \boldsymbol{Z}^{n+1}, \boldsymbol{P}^{n+1}, \boldsymbol{X}^{n+1}, \boldsymbol{V}^n\big) = 0, \quad 1 \le K \le N, 1 \le C \le \frac{d(d+1)}{2}, \tag{23d}$$

$$\mathcal{F}\boldsymbol{P}^k\big(\boldsymbol{U}^{n+1}, \boldsymbol{Z}^{n+1}, \boldsymbol{P}^{n+1}, \boldsymbol{X}^{n+1}, \boldsymbol{V}^n\big) = 0, \quad k \in \eta_P, \tag{23e}$$

where the mesh velocity is considered at time-step n without extrapolations.

5   DEFORMATION AND MESH ADAPTATION

To manage the collision stage, we use a short-range force $\mathbf{F}_{KJ}^{PP}$ between two particles B^K and B^J near contact, that is parallel to a vector joining its centers of mass, namely

$$\mathbf{F}_{KJ}^{PP} = \begin{cases} \mu \left(\frac{4\bar{R}}{d_{KJ}}\right)^{\frac{3}{2}} \left\|\mathbf{V}^J - \mathbf{V}^K\right\| \frac{\mathbf{X}_g^J - \mathbf{X}_g^K}{\left\|\mathbf{X}_g^J - \mathbf{X}_g^K\right\|} & \text{if} \quad d_{KJ} \le \delta \\ \mathbf{0} & \text{if} \quad d_{KJ} > \delta, \end{cases} \tag{24}$$

where δ (taken as $\bar{R}/10$) is the short-range in which $\mathbf{F}_{KJ}^{PP}$ acts, $\bar{R} = \min\left\{\bar{R}^K, \bar{R}^J\right\}$, being $\bar{R}^K$ de minimum distance between $\mathbf{x}_g^K$ and ∂B^K and $d_{KJ} > 0$ the distance between ∂B^K and ∂B^J. This results from solving a lubrication problem for a short-range gap, approximating as planar faces the boundaries of the solid bodies in collision process. Thereby, an additional body force given by

$$\mathbf{F}_K^{PP} = \sum_{J \neq K} \mathbf{F}_{KJ}^{PP},$$

is added up to the Newton-Euler equations (4) for the K-th solid.

Because of mesh deformation and the appearance of invalid elements through the simulation, mesh adaptation is adopted after each temporal step depending on a given tolerance $T > 0$, following the Algorithm 1. The mesh is adapted by means of topological operations applied to each *edge* of the triangulation $\mathcal{T}_h$: *collapsing* the *edge* to a point if the relative difference between its length and a comparative value E, corresponding to the average length of the edges

---

Algorithm 1: Mesh adaptation

Input   : Deformed mesh from $\mathcal{T}_h$, tolerance T
Output: Adapted mesh
for *all edge in $\mathcal{T}_h$* **do**
  $L \leftarrow$ length of *edge*;
  $E \leftarrow$ comparative value of *edge*;
  if $\frac{L-E}{E} < -T$ **then**
    collapse *edge*;
  else if $\frac{L-E}{E} > T$ **then**
    split *edge*;

---

attached to the *edge*'s end points, is smaller than $-T$, otherwise *splitting* the *edge* at its midpoint if the mentioned relative difference is greater than T. Typically we take $T = 0.7$.

If the mesh has been changed, either by removing or inserting nodes, all the flow fields (previously two or three calculated solutions defined over the old mesh), required to compute the next time step solution, are projected onto the adapted mesh. For a new node inserted at the midpoint of an edge, the average of the field at the end points of this edge is defined for the node. For a collapsed edge case, the value of one of its end points is maintained for the new node.

6 NUMERICAL RESULTS

6.1 Velocity field about a sphere

The Stokes equations result from neglecting inertial effects on a stationary version of the system (1). The derived linear problem can be numerically solved by the **BSS** (23) method with the mesh velocity prescribed as zero (no ALE terms), without body forces and the condition that there is not net force nor net torque acting on the fluid-solid system. These latter two assumptions are important characteristics of phoretic transport: external (electrical or temperature and concentration gradients) fields applies no force to the particle immersed in the Stokes flow (Anderson, 1989). We use this simplification to solve the flux around a solid sphere B, this is, a squirmer, of radius $R = 0.25$cm in which the slip velocity imposed $\mathbf{u}_s$ results from the tangential projection of the constant velocity field $\mathbf{Q}(x) = (-1\text{cm s}^{-1}, 0\text{cm s}^{-1}, 0\text{cm s}^{-1})$ to the eastern hemisphere (with respect to yz plane) as shown by Figure 2. In this case, the explicit formulae

$$\mathbf{V}_{\text{E}} = -\frac{1}{4\pi R^2} \int_B \mathbf{u}_s \, dS, \qquad \boldsymbol{\omega}_{\text{E}} = -\frac{3}{8\pi R^3} \int_B \mathbf{n} \times \mathbf{u}_s \, dS,$$

that relate the translational and angular velocities of the center of mass of the sphere with the slip velocity $\mathbf{u}_s$ in a unbounded medium (Fair and Anderson, 1989), give us the exact solution $\mathbf{V}_{\text{E}} = (3.333 \cdot 10^{-1}\text{cm s}^{-1}, 0\text{cm s}^{-1}, 0\text{cm s}^{-1})$ and $\boldsymbol{\omega}_{\text{E}} = (0\text{cm s}^{-1}, 0\text{cm s}^{-1}, 0\text{cm s}^{-1})$, which compared to the P_2/P_1 approximated solution, calculated in cuboidal domain of side length 200cm $= 800R$, namely $\mathbf{V}_{\text{N}} = (3.482 \cdot 10^{-1}\text{cm s}^{-1}, 3.627 \cdot 10^{-4}\text{cm s}^{-1}, 2.885 \cdot 10^{-5}\text{cm s}^{-1})$ and $\boldsymbol{\omega}_{\text{N}} = (9.036 \cdot 10^{-4}\text{cm s}^{-1}, 5.848 \cdot 10^{-4}\text{cm s}^{-1}, 1.060 \cdot 10^{-4}\text{cm s}^{-1})$, we found an absolute difference of 1.4% and 0.6%, respectively.
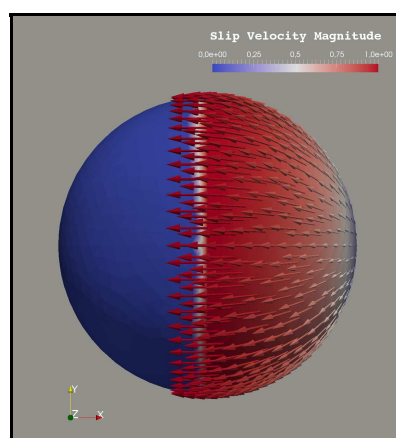

Figure 2: Slip velocity field over a sphere used to solve the Stokes problem

The slip velocity, that could be generated by the response of the particle to temperature or concentration gradients (thermophoresis and diffusiophoresis), electric fields (electrophoresis) or other phoretic phenomena, acts over the sphere's surface (a tangent vector field) and controls the dynamics of the surrounded fluid creating a difference between the fluid velocity and the particle's velocity. Because of this and the zero net force and torque on the particle, its velocity field is different from flows associated with particle sedimentation where external fields exerts a net force on it: for the squirmer case de velocity decays to zero as r^{-n}, with $n > 1$, meanwhile, in the sedimentation-like case the velocity decays as r^{-1}, being $r > 0$ the distance to the sphere center (Anderson, 1989). Figure 3 shows the streamlines restricted to the xy plane for the fluid-squirmer system against the streamlines for the same fluid-solid system but, instead of the slip velocity, the translational velocity $\mathbf{V}_{\mathrm{E}}$ has been imposed over the particle. Due to the presence of the domain walls two big circulation regions appear for the sedimentation-like case different from the squirmer case, in which four big circulation regions take place. Figure 4 compares the decay of the velocity field for these two cases: the magnitude of the velocity vector field decays faster in the squirmer case than in the pure translational case.
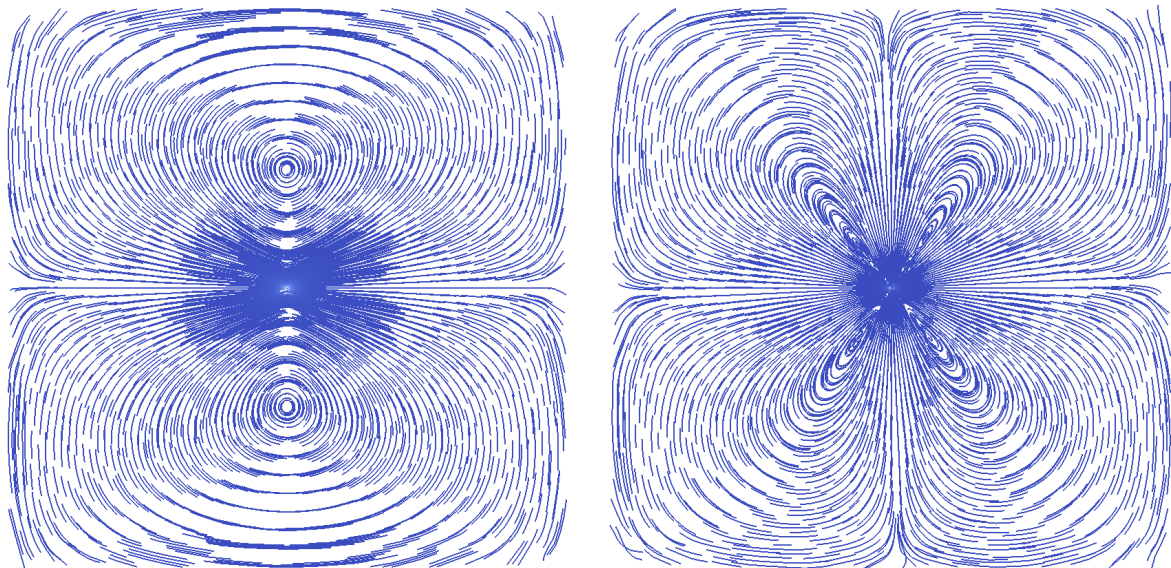
Figure 3: Streamlines of the Stokes flow about a sphere for the sedimentation-like case (left) and the squirmer case (right), the sphere is located at the center of the square

6.2 *Drafting*, *kissing* and *tumbling* of two particles

In this simulation two circular rigid bodies with densities $\rho_1 = \rho_2 = 1.50\mathrm{g\,cm^{-3}}$ and common diameter $D = 0.25\mathrm{cm}$, aligned one over the other in a channel of width $2.00\mathrm{cm}$ and height $6.00\mathrm{cm}$, interact following the well-known *drafting*, *kissing* and *tumbling* (DKT) phenomenon (Figure 6). These particles are immersed in a fluid of density $\rho_f = 1.00\mathrm{g\,cm^{-3}}$ and viscosity $\mu = 0.01\mathrm{g\,cm^{-1}\,s^{-1}}$. Under gravity effects (with $\mathbf{g} = (0.0\mathrm{cm\,s^{-2}}, -980.0\mathrm{cm\,s^{-2}})$) the lower disk (with center of mass initially at $\mathbf{x}_g^2 = (1.0\mathrm{cm}, 4.5\mathrm{cm})$), when falling, creates a pressure drop in its wake, allowing that the upper disk (initially at $\mathbf{x}_g^1 = (1.0\mathrm{cm}, 5.0\mathrm{cm})$) encounters less resistance from the fluid than the lower one and settles faster causing that the rigid bodies (almost) touch each other.
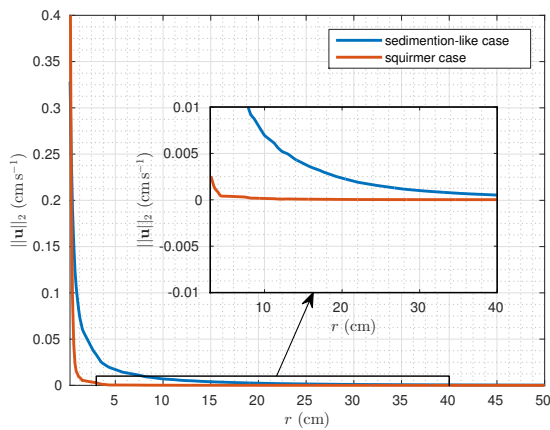
Figure 4: Decayment of the magnitude of the velocity vector field for the squirmer and sedimentation-like Stokes flow cases
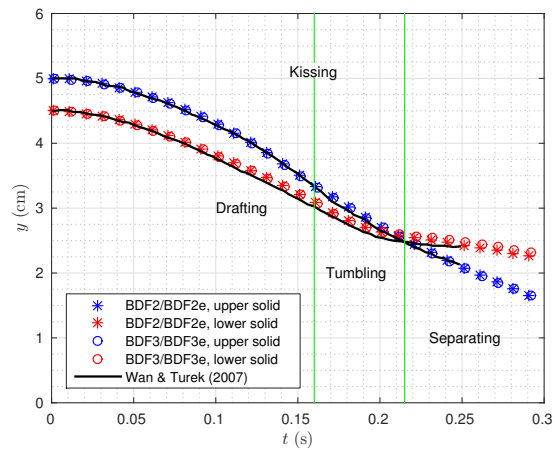
Figure 5: Time history of centers of mass of two circular rigid bodies compared to results obtained by Wan and Turek (2007)

Figure 5 shows the numerical results of using **BDF2/BDF2E** (20) and **BDF3/BDF3E** (22) methods to simulate de DKT phenomenon, compared to those of Wan and Turek (2007), presenting good agreement in the falling process. The velocity and pressure are approximated in the space P_1/P_1 with stabilization given by the Galerkin Least Squares (GLS) formulation (Hughes et al., 1986; Codina, 2001; Montefuscolo et al., 2014). As shown in Figure 6, some elements with bad aspect ratio could appear in the simulation that cannot be avoided if the adaptation of interfacial edges is not allowed, which is our case, however, this did not represent a problem for the simulation.
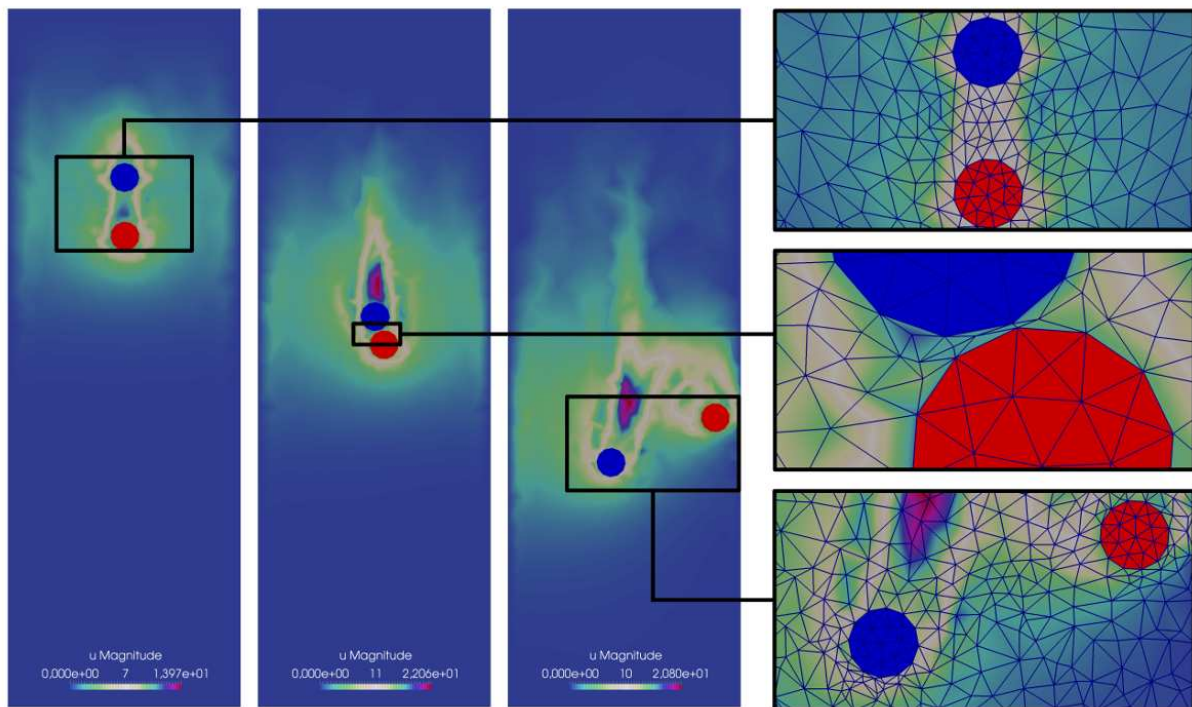
Figure 6: DKT of two particles in a vertical channel falling down by gravity effects, detailing mesh structure at instants $t = 0.08$s, 0.16s, 0.25s (left to right)

6.3   Fluid in an annular region

A system of two concentric circular pipes of radius R_1 and R_2, with $R_1 < R_2$, enclosing a viscous fluid is considered here. The outer pipe rotates about the common axis with constant angular velocity ω_2 while the inner pipe as well as the surrounded fluid are initially at rest.

Adopting a cylindrical coordinate system r, θ, z, in which the z-axis lies along the common axis of the pipes, and supposing sufficiently long pipes in order to neglect end effects, the only non-vanishing component of the fluid laminar velocity field is the tangential component u_θ that depends merely on the radius and time (due to incompressibility), while the radial and axial components, u_r and u_z respectively, are zero. In such manner, we seek a solution in the form

$$u_r = u_z = 0, \quad u_\theta = u\left(r, t\right),$$

thus, the Navier-Stokes equations (1) and Newton-Euler equations (4) form the reduced coupled system for the velocity field

$$\begin{cases} \rho_f \dfrac{\partial u}{\partial t} = \mu \dfrac{\partial}{\partial r}\left(\dfrac{1}{r}\dfrac{\partial\left(ru\right)}{\partial r}\right) & \text{for } R_1 < r < R_2, t > 0, \\[2mm] I_{33}\dfrac{d\omega}{dt} = 2\pi R_1^2\mu\left[r\dfrac{\partial}{\partial r}\left(\dfrac{u}{r}\right)\right]_{r=R_1} & \text{for } t > 0, \end{cases} \tag{25}$$

subject to initial, boundary and no-slip conditions

$$\begin{aligned} u\left(r,0\right) &= u_0\left(r\right) && \text{for } R_1 < r < R_2, \\ u\left(R_2, t\right) &= R_2\omega_2 && \text{for } t > 0, \\ u\left(R_1, t\right) &= R_1\omega\left(t\right) && \text{for } t > 0, \end{aligned}$$

where $\omega = \omega\left(t\right)$ is the angular velocity at time t of the inner pipe with inertia per unit length I_{33}, and u_0 is an initial radial velocity function.

Introducing the non-dimensional variables

$$\hat{u} = \frac{u}{U}, \ \hat{r} = \frac{r}{R_2}, \ \hat{t} = \frac{t\mu}{\rho_f R_2^2}, \ \hat{\omega} = \frac{\omega R_2}{U}, \ \hat{R}_1 = \frac{R_1}{R_2}, \ \hat{I} = \frac{I_{33}}{2\pi\rho_f R_1^2 R_2^2}$$

the parabolic problem (25) is transformed in the system

$$\begin{cases} \dfrac{\partial\hat{u}}{\partial\hat{t}} = \dfrac{\partial}{\partial\hat{r}}\left(\dfrac{1}{\hat{r}}\dfrac{\partial\left(\hat{r}\hat{u}\right)}{\partial\hat{r}}\right) & \text{for } \hat{R}_1 < \hat{r} < 1, \hat{t} > 0, \\[2mm] \hat{I}\dfrac{d\hat{\omega}}{d\hat{t}} = \left[\hat{r}\dfrac{\partial}{\partial\hat{r}}\left(\dfrac{\hat{u}}{\hat{r}}\right)\right]_{\hat{r}=\hat{R}_1} & \text{for } \hat{t} > 0, \end{cases} \tag{26}$$

with initial, boundary and no-slip conditions

$$\begin{aligned} \hat{u}\left(\hat{r}, 0\right) &= \hat{u}_0\left(\hat{r}\right) && \text{for } \hat{R}_1 < \hat{r} < 1, \\ \hat{u}\left(1, \hat{t}\right) &= \hat{\omega}_2 && \text{for } \hat{t} > 0, \\ \hat{u}\left(\hat{R}_1, \hat{t}\right) &= \hat{R}_1\hat{\omega}\left(\hat{t}\right) && \text{for } \hat{t} > 0, \end{aligned}$$

being U a characteristic velocity, $\hat{\omega}_2 = \frac{\omega_2 R_2}{U}$ and $\hat{u}_0\left(\hat{r}\right) = \frac{u_0(r)}{U}$.
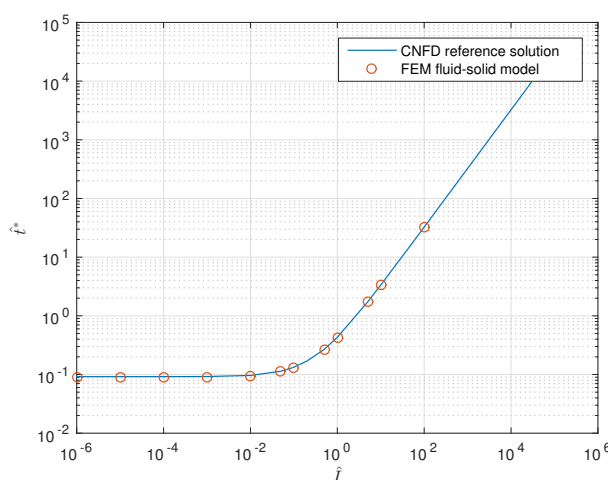
Figure 7: Non-dimensional time $\hat{t}^*$ as a function of $\hat{I}$ at which the solid attains half of the maximum angular velocity in logarithmic scale

Setting $U = 1\,\mathrm{cm\,s^{-1}}$, $R_2 = 1\mathrm{cm}$, $R_1 = 0.25R_2$, $\mu = 1\,\mathrm{g\,cm^{-1}\,s^{-1}}$, $\rho_f = 1\,\mathrm{g\,cm^{-3}}$ and $\omega_2 = 1\mathrm{rad\,s^{-1}}$, we obtain the non-dimensional inertia $\hat{I} = \frac{1}{64}\rho_1$, that is to say, it is proportional to the inner (solid) pipe non-dimensional density ρ_1. Figure 7 shows the non-dimensional time $\hat{t}^*$ at which the non-dimensional angular velocity $\hat{\omega}$ attains half of its maximum value, as a function of the non-dimensional inertia $\hat{I}$ calculated for several values of ρ_1 ranging from 10^{-6} to 10^2, all this in logarithmic scale. It has been used a Crank-Nicolson Finite Differences (CNFD) method to solve the non-dimensional system (26) in the spatial-temporal domain $[R_1, 1] \times [0, T]$, $T > 0$, and the **MR/AB** (19) method for the FEM fluid-solid model.

As expected, for small values of $\hat{I}$, this is, low solid density, the inner pipe experiences a high angular acceleration and reach quickly the stationary state as a consequence of its low resistance to tangential forces generated by the viscosity of the surrounding fluid moved by the outer pipe. On the other hand, if the non-dimensional inertia is increased, the internal solid gains more resistance to movement so it takes much longer to reach half of the maximum angular velocity.

With regard to temporal stability for the P_1/P_1 with GLS stabilization and characteristic spatial length $h = 0.01$, the maximum time step for **MR/AB** (19), **BDF2/BDF2E** (20), **BDF2/AB** (21), **BDF3/BDF3E** (22) and **BSS** (23) is, respectively, 0.06, 0.110, 0.108, 0.113 and 0.025. Similar to that reported by Montefuscolo et al. (2014), the staggered scheme is more restrictive in the allowed time step for stability, meanwhile the extrapolated versions of the backward differences schemes allow larger time steps.

Now, for the same annular geometry but with $\mu = 0.01\,\mathrm{g\,cm^{-1}\,s^{-1}}$, $\rho_f = 1\,\mathrm{g\,cm^{-3}}$ and $\rho_1 = 1.25\,\mathrm{g\,cm^{-3}}$, we have chosen the time steps $\Delta t = 0.05 \cdot 2^{-k}$, $k = 0, 1, 2, 3, 4$ to evaluate the convergence order of the numerical methods. The velocity error $E = \|\mathbf{u}\,(t^n, \cdot) - \mathbf{u}_h^n\,(\cdot)\|_{L^2(\Omega_h(t^n))}$ has been calculated at time $t^n = 0.8\mathrm{s}$ for each time step and the results are summarized in the Table 1. Again, we consider as an "exact" reference velocity $\mathbf{u}$ the one obtained by solving with CNFD method the system (26). The expected orders 2 and 3 were achieved for **BDF2/AB** and **BDF3/BDF3E**, respectively, in the last tests. In the case of **MR/AB** the last test showed a better converge order. Finally, for the **BDF2/BDF2E** the last order result is in need of verification.

k	**MR/AB**	Order	**BDF2/BDF2E**	Order
0	5.5839e-02		4.8643e-02	
1	2.7349e-02	1.0297	1.4622e-02	1.7340
2	1.3514e-02	1.0171	3.7499e-03	1.9633
3	6.6154e-03	1.0306	9.3618e-04	2.0020
4	2.0392e-03	1.6978	5.9122e-04*	0.6631*

k	**BDF2/AB**	Order	**BDF3/BDF3E**	Order
0	7.2598e-02		1.2816e-01	
1	3.7336e-02	0.9593	6.7750e-02	0.9197
2	1.8516e-02	1.0118	3.0934e-02	1.1310
3	5.2342e-03	1.8228	4.1583e-03	2.8952
4	1.2755e-03	2.0369	6.9390e-04	2.5832

Table 1: Convergence order for the presented numerical schemes. *Result in need of verification

6.4 Diffraction of squirmers by passive particles

This numerical simulation studies the change in the trajectory of a squirmer particle when it passes near a passive one. Assuming both particles to be circular (2D) of radius R, the problem is completely determined by the non-dimensional ratio $\kappa = e/R$, where e is the distance from the unperturbed (rectilinear) squirmer trajectory to the initial position of the passive particle. The problem is rendered non-dimensional by scaling length with R and time with R/v^*, where v^* is the unperturbed squimer's velocity.

Trajectories of the particles for some values of κ are shown in Figure 8. It is evident that the particles experience a collision-like movement mediated by hydrodynamic interactions. The post-collision state is defined by (a) the angular orientation of the squirmer $\theta(t \to \infty)$, and (b) the final position of the passive particle $\mathbf{x}_g^1(t \to \infty)$. Figures 9 and 10 show these variables as functions of non-dimensional time $\hat{t} = tv^*/R$. For $\kappa = 0.0$, asymmetries in the mesh results in
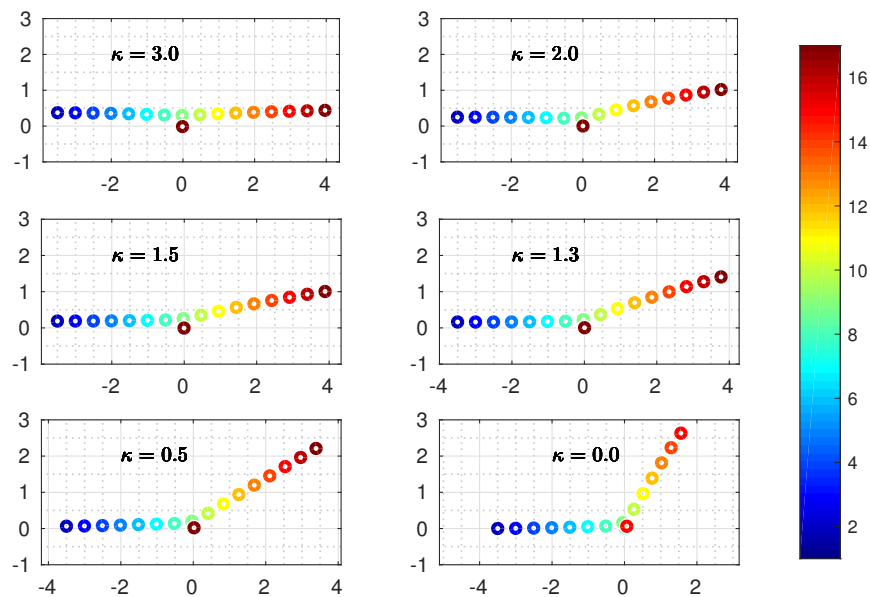

Figure 8: Trajectory of the active squirmer for several values of κ. The color scale corresponds to the time in seconds
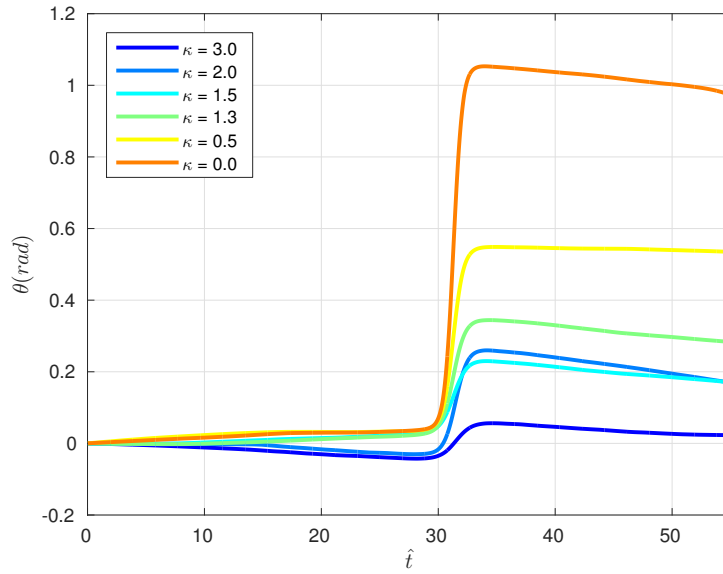
Figure 9: Angular orientation advancing of the active squirmer in non-dimensional time for several values of κ

a collision that sends away the squirmer from the passive particle, i.e. the active particle leaves the axis x, like in the other cases. Details of the collision with the instantaneous velocity fields are shown in Figure 11 for $\kappa = 1.3$: the passive particle returns to its initial position once the squirmer moves away from it.

For the simulations we have taken $R = 0.125$cm, $v^* = 0.49$cm s^{-1}, the passive particle is initially located at the origin of coordinates $\mathbf{x}_g^1(0) = \mathbf{0}$ and the active one at $\mathbf{x}_g^2(0) = (-4\text{cm}, e)$ and slip velocity $\mathbf{u}_s$ given by the tangential projection of the constant velocity field $\mathbf{Q}(\mathbf{x}) = (-1\text{cm s}^{-1}, 0\text{cm s}^{-1})$ over its boundary. These particles are immersed in a fluid with $\mu = 1$g cm^{-1} s^{-1} and $\rho_f = 1$g cm^{-3} without body forces acting over the system. The active squirmer moves and changes its swimming direction due to the presence of the passive particle, depending on its initial position controlled by κ (Figure 8), at the same time the passive particle changes its position in response of the squirmer proximity as shown in Figure 11.
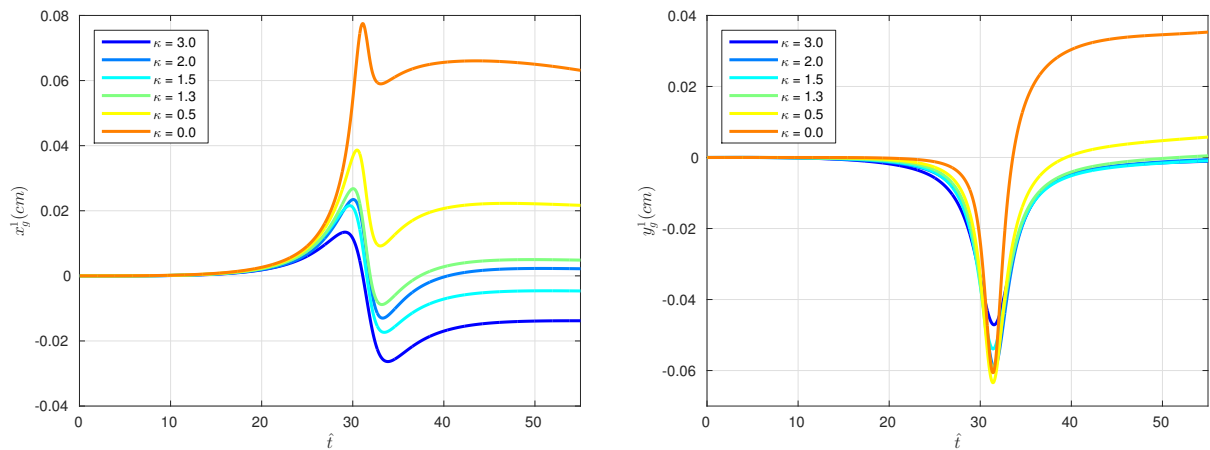

Figure 10: Position of the passive particle $\mathbf{x}_g^1$ in non-dimensional time for several values of κ: x_g^1-component (left) and y_g^1-component (right)
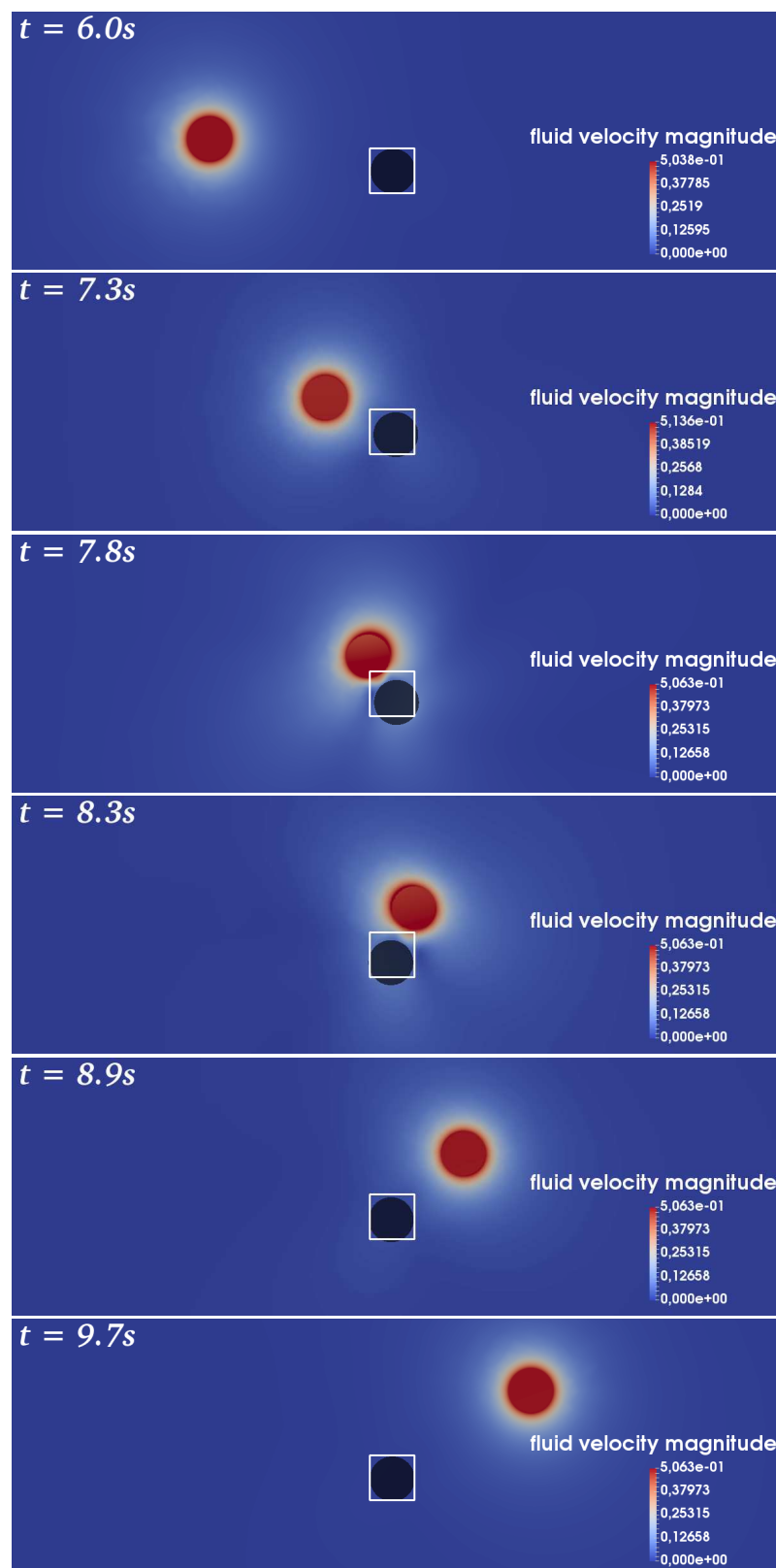
Figure 11: Velocity magnitude of the fluid for several times showing the (almost) collision stage, for $\kappa = 1.3$. The white square delimits the unperturbed position of the passive (shadowed) particle

7 CONCLUSIONS

We have shown an extension of the ALE schemes introduced by Montefuscolo et al. (2014) for the fluid-solid interaction. The weak formulation of the coupling of the Newton-Euler equations to the Navier-Stokes system through surface forces, turned out into a DAE system discretized in space by P_2/P_1 and P_1/P_1 with GLS stabilization, and in time by several geometry extrapolation techniques, resulting in stable numerical methods of different orders in time. Also, we have introduce the slip velocity in the fluid-solid model, being able to simulate the dynamics of squirmers.

8 ACKNOWLEDGEMENTS

REFERENCES

Anderson J.L. Colloid transport by interfacial forces. *Annual review of fluid mechanics*, 21(1):61–99, 1989.

Codina R. A stabilized finite element method for generalized stationary incompressible flows. *Computer Methods in Applied Mechanics and Engineering*, 190(20):2681–2706, 2001.

Day M.A. The no-slip condition of fluid dynamics. *Erkenntnis*, 33(3):285–296, 1990.

Fair M. and Anderson J. Electrophoresis of nonuniformly charged ellipsoidal particles. *Journal of colloid and interface science*, 127(2):388–400, 1989.

Glowinski R., Pan T., Hesla T., Joseph D., and Periaux J. A fictitious domain approach to the direct numerical simulation of incompressible viscous flow past moving rigid bodies: application to particulate flow. *Journal of Computational Physics*, 169(2):363–426, 2001.

Golestanian R., Liverpool T.B., and Ajdari A. Propulsion of a molecular machine by asymmetric distribution of reaction products. *Physical review letters*, 94(22):220801, 2005.

Hu H.H., Patankar N.A., and Zhu M. Direct numerical simulations of fluid–solid systems using the arbitrary lagrangian–eulerian technique. *Journal of Computational Physics*, 169(2):427–462, 2001.

Hughes T.J., Franca L.P., and Balestra M. A new finite element formulation for computational fluid dynamics: V. circumventing the babuška-brezzi condition: A stable petrov-galerkin formulation of the stokes problem accommodating equal-order interpolations. *Computer Methods in Applied Mechanics and Engineering*, 59(1):85–99, 1986.

Jülicher F. and Prost J. Generic theory of colloidal transport. *The European Physical Journal E*, 29(1):27–36, 2009.

Khair A.S. and Squires T.M. The influence of hydrodynamic slip on the electrophoretic mobility of a spherical colloidal particle. *Physics of Fluids (1994-present)*, 21(4):042001, 2009.

Montefuscolo F., Sousa F.S., and Buscaglia G.C. High-order ale schemes for incompressible capillary flows. *Journal of Computational Physics*, 278:133–147, 2014.

Popescu M.N., Dietrich S., Tasinkevych M., and Ralston J. Phoretic motion of spheroidal particles due to self-generated solute gradients. *The European Physical Journal E*, 31(4):351–367, 2010.

Ruckenstein E. and Dunn C. Slip velocity during wetting of solids. *Journal of Colloid and Interface Science*, 59(1):135–138, 1977.

Saintillan D. Nonlinear interactions in electrophoresis of ideally polarizable particles. *Physics*

of Fluids (1994-present), 20(6):067104, 2008.

Wan D. and Turek S. Fictitious boundary and moving mesh methods for the numerical simulation of rigid particulate flows. *Journal of Computational Physics*, 222(1):28–56, 2007.

Yang M., Wysocki A., and Ripoll M. Hydrodynamic simulations of self-phoretic microswimmers. *Soft matter*, 10(33):6208–6218, 2014.